
Filament Recycling and Sustained Contractile Flows in an Actomyosin Cortex

William McFadden¹, Jonathan Michaux², Patrick McCall³, Edwin Munro^{2,*}

1 Biophysical Sciences Program, University of Chicago, Chicago, IL, USA

2 Department of Molecular Genetics and Cell Biology, University of Chicago, Chicago, IL, USA

3 Department of Physics, University of Chicago, Chicago, IL, USA

* emunro@uchicago.edu

Abstract

Fill in abstract later.

Author Summary

In this paper, we develop and analyze a minimal model for 2D active networks based on the cortical cytoskeleton of eukaryotic embryos. Our model introduces a drag-like slip between cross-linked filaments as means to dissipate stored stress, generating a macroscopic effective viscosity. We further introduce an active friction to active stress from microscopic properties. We generate computational simulations based on the model, and demonstrate that active stress is sufficient to drive network contraction only temporarily. By introducing filament recycling, we are able to set up steady state flow profiles such as those found in the cortex of developing embryos and migrating cells. The model is used to calculate phenomenological constants measured in prior experiments. Our analysis sheds insight on potential microscopic control parameters governing broad qualitative differences in 2D active networks. We make our model freely accessible and our methodology transparent to enable other researchers to clearly understand our modeling framework and to build upon our findings.

Introduction

Cortical flow is a fundamental and ubiquitous form of cellular deformation that underlies cell polarization, cell division, cell crawling and multicellular tissue morphogenesis [Bray and White, 1988, Hird and White, 1993]. These flows arise within the actomyosin cortex, a thin layer of cross-linked actin filaments and myosin motors that lies just beneath the plasma membrane [Salbreux et al., 2012]. The active forces that drive cortical flows are thought to be generated by myosin motors pulling against individual actin filaments [Munro et al., 2004]. These forces must be integrated within cross-linked networks to build macroscopic contractile stress. At the same time, cross-linked networks resist deformation and this resistance must be dissipated by network remodeling to allow macroscopic network deformation and flow. How force production and dissipation depend on motor activity, network architecture and remodeling remains poorly understood.

Current models for cortical flow rely on coarse-grained descriptions of actomyosin networks as active fluids, whose motions are driven by gradients of active contractile stress and opposed by an effectively viscous resistance [Mayer et al., 2010]. In these models, gradients of active stress are assumed to reflect spatial variation in motor activity and viscous resistance is assumed to reflect the internal dissipation of elastic resistance due to local remodeling of filaments and/or crosslinks [Bois et al., 2011]. A key virtue of these models is that their behavior is governed by a few parameters (active stress and effective viscosity). By coupling an active fluid description to simple kinetic models for network assembly and disassembly and making active stress and effective viscosity depend on e.g network density and turnover rates, it is possible to capture phenomenological descriptions of cortical flow. Models based on this active fluids description can successfully reproduce spatiotemporal dynamics of cortical flow observed during polarization [Mayer et al., 2010], cell division [Turlier et al., 2014, Salbreux et al., 2009], cell motility [Keren et al., 2009, Marchetti et al., 2013] and tissue morphogenesis [Heisenberg and Bellaïche, 2013].

However, to understand how cells exert physiological control over cortical deformation and flow, or to build and tune networks with desired properties *in vitro*, it is essential to connect this coarse-grained description to the microscopic origins of force generation and dissipation within cross-linked actomyosin networks. Both active stress and effective viscosity depend sensitively on microscopic parameters including densities of filaments, motors and cross-links, force-dependent motor/filament interactions, cross-link dynamics and network turnover rates. Thus a key challenge is to understand how tuning these microscopic parameters controls the dynamic interplay between active force generation and passive relaxation to control macroscopic dynamics of cortical flow.

Studies in living cells have documented fluid-like stress relaxation on timescales of 10-100s of seconds [Mayer et al., 2010, Hird and White, 1993, Bray and White, 1988, Hochmuth, 2000, Evans and Yeung, 1989, Bausch et al., 1998]. These modes of stress relaxation are thought to arise both from the transient binding/unbinding of individual cross-links and from the turnover (assembly/disassembly) of actin filaments (ref). Studies of cross-linked and/or bundled actin networks *in vitro* suggest that cross-link unbinding may be sufficient to support viscous relaxation (creep) on very long timescales [Wachsstock et al., 1994, Lieleg et al., 2008, Lieleg et al., 2009, Yao et al., 2011, Liu et al., 2007], but is unlikely to explain the rapid large scale cortical deformation and flow observed in living cells. suggest that rapid actin turnover must play a significant role as well. Indeed, photokinetic and single molecule imaging studies reveal rapid turnover of cortical actin filaments in living cells on timescales of 10-100 seconds [Robin et al., 2014]. Previous theoretical models have explored the dependence of stress relaxation on cross-link binding and unbinding analytically [Broedersz et al., 2010, Müller et al., 2014] and others have explicitly modeled reversible cross-linking in combination with complex mechanics of filament bundles [Kim et al., 2011, Lieleg et al., 2009, Lieleg and Bausch, 2007]. However, until very recently [Mak et al., 2016] very little attention has been paid to actin turnover as mechanism of stress relaxation.

Recent work has also begun to reveal insights into mechanisms that govern active stress generation in disordered actomyosin networks. In vitro studies have confirmed that local interactions among actin filaments and myosin motors are sufficient to drive macroscopic contraction of disordered networks [Murrell and Gardel, 2012]. Theoretical studies suggest that asymmetrical compliance of actin filaments (stiffer under extension than compression) and spatial differences (dispersion) in motor activity are sufficient conditions for contraction in one [Lenz et al., 2012] and two [Lenz, 2014] dimensional networks, although other routes to contractility may also exist [Lenz, 2014]. Further work has explored how modulation of network architecture, crosslink dynamics and

motor density, activity and assembly state can shape rates and patterns of network deformation [Köhler and Bausch, 2012, Alvarado et al., 2013, Banerjee and Marchetti, 2011] or network rheology [Liverpool et al., 2009, Koenderink et al., 2009].

Significantly, *in vitro* models for disordered actomyosin networks have used stable actin filaments, and these networks support only transient contraction, either because of network collapse (ref), or buildup of elastic resistance (ref?), or because network rearrangements (polarity sorting) dissipate the potential to generate contractile force (ref). This suggests that continuous turnover of actin filaments may play a key role in allowing sustained deformation and flow (refs). Recent theoretical and modeling studies have begun to explore how this could work [Hiraiwa and Salbreux, 2015, Mak et al., 2016, Zundieck et al., 2007], and to explore dynamic behaviors that can emerge in contractile material with turnover [Dierkes et al., 2014]. However, there is much to learn about how the buildup and maintenance of contractile force during continuous deformation and flow depends on local interplay of network architecture, motor activity and filament turnover.

The goal of this work was to build a computational bridge between the microscopic description of cross-linked actomyosin networks and the coarse grained macroscopic description of an active fluid. We sought to capture the essential microscope features (dynamic cross-links, active motors and semi flexible actin filaments with asymmetric compliance and continuous filament recycling), but in a way that is sufficiently simple to allow systematic exploration of how parameters that govern network deformation and flow in an active fluid theory depend on microscopic parameters. To this end, we introduce several coarse-grained approximations into our representation of filament networks. First, we represent semi-flexible actin filaments as chains of simple springs with asymmetric compliance (stronger in extension than compression). Second, we replace dynamic binding/unbinding of elastic cross-links with a coarse-grained representation in terms of molecular friction [Vanossi et al., 2013, Spruijt et al., 2010, Filippov et al., 2004], such that filaments can slide past each other against a constant frictional resistance. Third, we used a similar scheme to introduce active motors at filament crossover points with a simple linear force/velocity relationship, and we introduce ?dispersion? of motor activity by making only a subset of filament overlaps active [Banerjee et al., 2011]. Finally, we model filament turnover by regularly resetting a subset of filaments to a new unstrained position. Importantly, these simplifications allow us to extend our single polymer models to dynamical systems of larger network models for direct comparison between theory and modeling results. This level of coarse graining will therefore make it easier to understand classes of behavior for varying compositions of cross-linked filament networks. In addition, it allows us to compute a new class of numerical simulations efficiently, which gives us concrete predictions for behaviors in widely different networks with measurable dependencies on molecular details.

Models

We choose to focus our attention on 2D networks both for their tractability as well as their relevance in the quasi-2D cytoskeletal cortex of many eukaryotic cells [Mayer et al., 2010]. In addition, recent developments in 2D *in vitro* systems [Murrell and Gardel, 2012, Sanchez et al., 2012], make 2D disordered models all the more interesting as a renewed focus of study. In the rest of this section, we underline the key points necessary for understanding our modeling framework and the key assumptions we have made in generating our equations of motion for the system.



Figure 1. Schematic of modeling framework. a) Filaments are represented as connected chains of spring-like segments with asymmetric compliance. segments have a smaller spring constant for compression than for extension. b) Cross-linking is represented as filament coupling by an effective drag, such that their relative motion is proportional to any applied force. c) Motor activity manifests as a basal sliding rate even in the absence of an external force. d) Only a subset of filament cross-links are active, resulting in differential force exertion along the filament. e) Filaments are turned over at a constant rate, leading to a refreshing in the strain state of all filaments after a characteristic timescale.

Asymmetric Filament Compliance

We model individual filaments as chains of springs with relaxed length l_s . Filaments can therefore be represented as a sequence of nodes with positions \mathbf{x}_i and nearest neighbor force interactions, \mathbf{F}_i^μ , of the form

$$|F_i^\mu| = \mu \cdot \frac{|\mathbf{x}_{i+1} - \mathbf{x}_i| - l_s}{l_s} + \mu \cdot \frac{|\mathbf{x}_{i-1} - \mathbf{x}_i| - l_s}{l_s} \quad (1)$$

where, μ represents an extensional modulus of a filament. Here, we take the modulus, μ , to have a different value depending on whether $|\mathbf{x}_{i-1} - \mathbf{x}_i| - l_s$ is greater or less than 0. This moduli is a composite quantity related to both filament and cross-linker compliance in a manner similar to a proposed effective medium theory [Broedersz et al., 2009]. In the limit of highly rigid cross-links and flexible filaments, our model reduces to the pure semi-flexible filament models of [Head et al., 2003, Wilhelm and Frey, 2003]. In the opposite regime of nearly rigid filaments and highly flexible cross links, our method is still largely similar to the model of [Broedersz et al., 2009] in small strain regimes before any nonlinear cross link stiffening. However, in departure from those models, the magnitude of the force on interior cross-links in our model is still the same as those on the exterior. This is a simplification of the varying levels of strain that would actually be present in these cross-linkers as addressed in [Broedersz et al., 2009], but we choose to ignore the slight variation in favor of an approximated, global mean approach.

Drag-like Coupling Between Overlapping Filaments

Cross-link binding and unbinding is an important element of the overall stress relaxation of a network. In contrast to previous models, we allow relaxation of the network's stored stress by letting the attachment points slip. We do this by replacing an elastic interaction between pairs of points along filament segments with a drag-like coupling between segments.

$$\mathbf{F}_i^\xi = \xi \cdot \int_{s_{i-1}}^{s_{i+1}} ds \frac{l_s - |s - s_i|}{l_s} (\mathbf{v}_i - \mathbf{v}_j) p_{ij}(s) \quad (2)$$

Where $p_{ij}(s)$ represents the locational distribution of cross-link points (equal to 1 at locations of cross-links and 0 elsewhere) and \mathbf{v}_i and \mathbf{v}_j represent the the velocities of the i th and j th filament segment. This model assumes a linear relation between applied force and the velocity difference between attached segments. This drag-like coupling has been shown to be an adequate approximation in the case of ionic cross-linking of actin [Ward et al., 2015, Chandran and Mofrad, 2010], and can be found in the theoretical basis of force-velocity curves for myosin bound filaments [Banerjee et al., 2011]. Although non-linearities can arise through force dependent detachment kinetics and/or non-linear force extension of cross-links, we assume that inhomogeneities from non-linear effects are of second or higher order. With this assumption, the motion for the entire network is governed by a dynamical equation of the form

$$L\zeta\mathbf{v}_i + \mathbf{F}_i^\xi = \mathbf{F}_i^\mu \quad (3)$$

Here, the first term in the integral is the filament's intrinsic drag through its embedding fluid, ζ , while the second comes from the drag-like coupling between filaments, ξ .

Active Coupling for Motor Driven Filament Interactions

To add motor activity we select a subset of cross-linked points and impart an additional force of magnitude v directed in the orientations of the individual filaments, \mathbf{u}_i . This leads to a modification of the equation of motion to

$$\mathbf{F}_i^v = \hat{\mathbf{u}}_i \cdot v \int ds \sum_j \frac{l_s - |s - s_i|}{l_s} p_{ij} q_{ij} \quad (4)$$

In this formulation, only at the subset of points where $p_{ij} = 1$ and $q_{ij} = 1$ will there be a force imparted. In our simulations we let q_{ij} be selected randomly such that $\bar{q} = \phi$, where \bar{q} indicates the mean of q .

$$L\zeta \mathbf{v}_i + \mathbf{F}_i^\xi = \mathbf{F}_i^\mu + \mathbf{F}_i^v \quad (5)$$

2D Network Formation

We follow a mikado model approach by initializing a minimal network of connected unstressed linear filaments in a rectangular 2D domain. We generate 2D networks of these semi-flexible filaments by laying down straight lines of length, L , with random position and orientation. We then assume that some fixed fraction of overlapping filaments become cross-linked (defined in) at their point of overlap.

Although real cytoskeletal networks may form with non-negligible anisotropy, we focus on isotropically initialized networks for simplicity. We define the density using the average distance between cross-links along a filament, l_c . A simple geometrical argument can then be used to derive the number of filaments filling a domain as a function of L and l_c [Head et al., 2003]. Here, we use the approximation that the number of filaments needed to tile a rectangular domain of size $W \times H$ is $2WH/Ll_c$, and that the length density is therefore $1/l_c$. In the absence of cross-link slip, we expect the network to form a connected solid with a well defined elastic modulus [Head et al., 2003, Wilhelm and Frey, 2003].

System of Equations for Applied Stress

We model our full network as a coupled system of differential equations satisfying 5. Although the general mechanical response of this system may be very complex, we focus our attention on low frequency deformations and the steady-state creep response of the system to an applied stress. To do this we introduce a fixed stress, σ along one edge of the network. The stress is applied by applying individual forces to the filaments lying within a patch of size D_w such that the sum of individual forces is equal to the applied stress times the height of the domain. These forces points in the direction, $\hat{\mathbf{x}}$, producing and extension of the patch.

Finally, we add a 0 velocity constraint at the other edge of our domain of interest. We assume that our network is in the "dry," low Reynold's number limit, where inertial effects are so small that we can equate our total force to 0. Therefore, we have a dynamical system of wormlike chain filaments satisfying

$$L\zeta \mathbf{v}_i + \mathbf{F}_i^\xi(\mathbf{v}_i) = \mathbf{F}_i^\mu(\mathbf{x}_i) + \mathbf{F}_i^v(\mathbf{x}_i) + \sigma \hat{\mathbf{u}}(\mathbf{x}_i) \quad (6)$$

subject to constraints such that $\mathbf{v}_i(\mathbf{x})$ is 0 with $x = 0$. This results in an implicit differential equation for filament segments which can be discretized and integrated in time to produce a solution for the motion of the system.

Filament Recycling as a model for rapid filament turnover

To simplify the complex biochemical changes that can give rise to actin filament polymerization and depolymerization, we chose to use simple filament appearance and disappearance as a lowest order model of filament recycling. In this sense the average lifetime of a filament between it's appearance and disappearance would be τ_r . In order to do this without causing an unnecessary bias in the results, at a regularized interval $\tau_s < 0.01 \cdot \tau_r$, we selected τ_s/τ_r filaments, reset their extension or compression to 0, and relocated them to a random position and orientation. This has the effect of creating an approximately exponential decay in the number of old filaments over time.

Computational Simulation Method

We tested our analytical conclusions on a computational model. More technical details of the model can be found in the Appendix, but we summarize the main modeling points here.

We discretize the filaments such that the equations of motion becomes a coupled system of equations for the velocities of filament endpoints, \mathbf{x} . The drag-like force between overlapping filaments results in a coupling of the velocities of endpoints.

$$\mathbf{A} \cdot \dot{\mathbf{x}} = \mathbf{f}(\mathbf{x}) \quad (7)$$

where \mathbf{A} represents a coupling matrix between endpoints of filaments that overlap, and $\mathbf{f}(\mathbf{x})$ is the spring force between pairs of filament segment endpoints. We can then numerically integrate this system of equations to find the time evolution of the positions of all filament endpoints.

We generate a network by laying down filaments with random position and orientation within a domain of size D_x by D_y with periodic boundaries in the y-dimension. The external stress (shear or extensional/compressional) is applied to all filament endpoints falling within a fixed x-distance from the center of the domain. Finally, filament endpoints falling within a fixed x-distance from the edges of the domain are constrained to be nonmoving. All filament interactions, force fields, and constraints are smoothed over small regions such that the equations will contain no sharp discontinuities.

The nominal units for length, force, and time are μm , nN, and s, respectively. We explored parameter space around an estimate of biologically relevant parameter values, given in Table 1.

Table 1. Simulation Parameter Values

| parameter | symbol | physiological estimate |
|-----------------------------|------------------|------------------------------|
| extensional modulus | μ_e | $10nN$ |
| compressional modulus | μ_c | $0.1nN$ |
| cross-link drag coefficient | ξ | <i>unknown</i> |
| medium drag coefficient | ζ | $0.0005 \frac{nNs}{\mu m^2}$ |
| filament length | L | $5\mu m$ |
| cross-link spacing | l_c | $0.5\mu m$ |
| domain size | $D_x \times D_y$ | $20 \times 50\mu m$ |

Results and Discussion

We used our model to characterize how rates and patterns of cortical flow are shaped by complex dependencies of active force generation and passive force dissipation on network architecture, local coupling (active and passive) between filaments and filament recycling. We proceeded in three steps: First, we analyze the passive deformation of a network in response to a constant external force. We determine the timescales on which fluidlike deformation occurs as a function of network architecture and filament recycling times. Next, we considered the active case and made similar measurements of the timescales of internal stress buildup and dissipation. Finally, we were able to synthesize our understanding of the passive and active systems to analyze the behavior of a more complex situation of an actively flowing network.

Filament recycling prevents cortical tearing and modulates the viscous stress relaxation of passive filament networks

Networks with passive cross-links and no filament turnover undergo three stages of deformation in response to an extensional force. To characterize the passive response of a filament network with effective crosslink drag in the absence of filament recycling and motor activity, we imposed an external force on a simulated network, and then quantified network deformation and internal network stress as a function of time. An example of such simulations is shown in Figure 2a. We measured the local velocity of the network at different positions along the axis of deformation as the mean velocity of all filament segments intersecting that position; We measured the internal network stress at each position by summing the axial component of the tensions on all filament segments intersecting that position, and dividing by network height; finally, we measured network strain rate as the change in filament position length divided by its original position.

We found in our measurements of instantaneous stress and velocity (Figure 2b) that the network deforms nearly continuously. During intermediate stages of the deformation, the stress profile (blue) is nearly constant throughout the material while the velocity profile (orange) is linear in space. This justifies a material description in terms of bulk quantities.

Plotting the material stress and strain rates as function of time revealed that the deformation occurred in three qualitatively distinct phases (Figure 2a,c). On short timescales the network exhibited a rapid viscoelastic response, characterized by a rapid buildup of internal stress and a rapid exponential approach to a fixed strain similar to that predicted by [Head et al., 2003]. On intermediate timescales, the internal stress remained constant while the network continued to deform slowly and continuously with nearly constant strain rate as filaments slipped past one another against the effective drag. This linear relationship between strain and time characterizes a material with an effective viscosity, η_c , given by the ratio of the applied stress to the strain rate. We define the transition time between this fast, viscoelastic response and the slower, effectively viscous deformation phase as (τ_c) . Finally, on long timescales, this effectively viscous behavior broke down. As the network strain approached a critical value ($\sim 30\%$ for the simulation in Figure 2), strain thinning led to decreased network connectivity, local tearing, and acceleration of the network deformation (see inset in Figure 2c). This eventually resulted in the highly heterogeneous network structure shown in the $t=440$ example of Figure 2a.

Network architecture sets the rate and timescales of deformation. To better understand the origins of effective viscosity and the timescale for transition to viscous behavior and the effective viscosity, we systematically varied network parameters and applied stress and measured effective viscosity and the transition time (τ_c) . For the entire range of network parameters that we sampled, we observed a transition from a fast viscoelastic response to slow effectively viscous deformation. A simple theoretical analysis predicted that the effective viscosity should be proportional to the square of the crosslink density and the effective crosslink drag coefficient of the individual cross-links, with a constant of proportionality $\pi/4$. As shown in Figure 3a, our simulations agree well with the theory for a large range of network parameters. For many simple viscoelastic materials, the ratio of the elastic modulus, G_0 , to the viscosity η_c , is a general indicator of the transition timescale from elastic to viscous behavior (need a reference). Using the approximation of the equation for elastic modulus from [Head et al., 2003], $G_0 \approx \mu/l_c$, we predict a crossover time, $\tau_c \approx L^2\xi/l_c\mu$. By measuring the time at which the strain rate became nearly constant we obtained an estimate of this time for a wide variety of simulation parameters. As shown in Figure

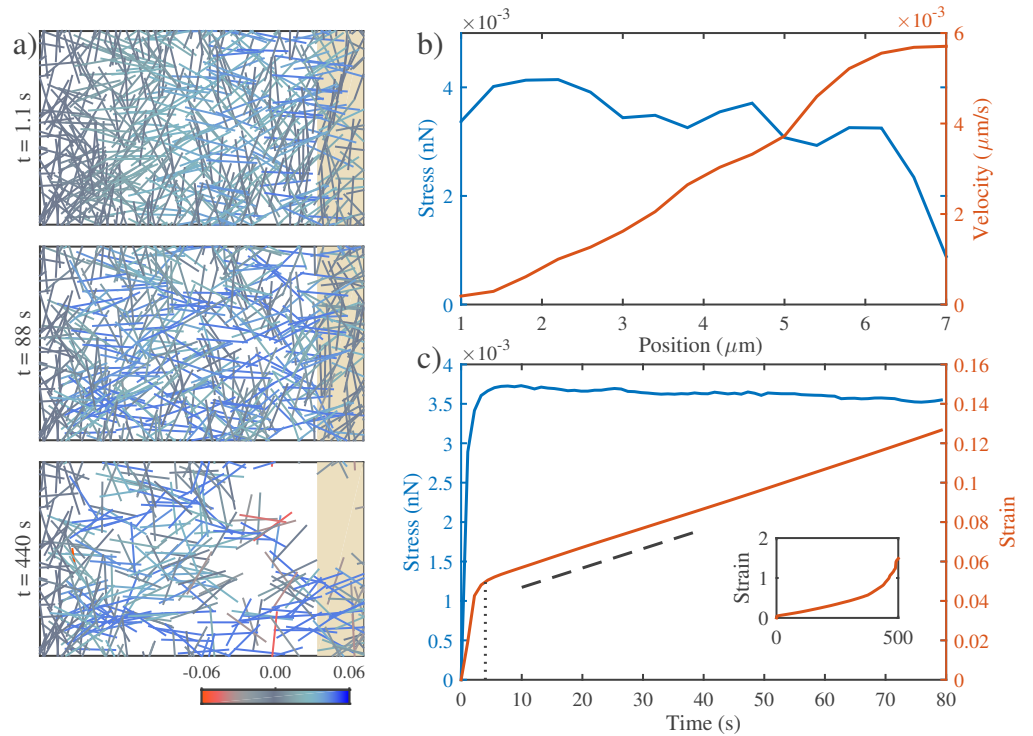


Figure 2. Networks with passive cross-links and no filament turnover undergo three stages of deformation in response to an extensional force. **a)** Three successive time points from a simulation of a $4 \times 10 \mu\text{m}$ network deforming under an applied extensional stress of $0.005 \text{ nN}/\mu\text{m}$. In this and all subsequent figures, filaments are color-coded with respect state of stress (blue = tension, red = compression). Network parameters: $L = 1 \mu\text{m}$, $l_c = 0.3 \mu\text{m}$, $\xi = 100 \text{ nN} \cdot \text{s}$. **b)** Mean filament stress and velocity profiles for the network in (a) at $t=88\text{s}$. Note that the stress is nearly constant and the velocity is nearly linear as predicted for a viscous fluid under extension. **c)** Plots of the mean stress and strain vs time for the simulation in (a), illustrating the three stages of deformation: (i) A fast initial phase accompanies rapid buildup of internal network stress; (ii) after a characteristic time τ_c s (indicated by vertical dotted line) the network deforms like a material with a constant effective viscosity, η_c , as indicated by the slope of the dashed line. (inset) At long times, the strain accelerates as the network undergoes strain thinning and eventually tears.

3b, our approximation is in good agreement with the observed transition time. These data confirm that our model is consistent with previous models for the viscoelastic response of semi flexible polymer networks.

Filament recycling rescues network tearing and modulates effective viscosity. We next explored how the passive network response to an applied force changed in the presence of filament recycling. To do so we ran a series of simulations with identical filament lengths and network densities and filament slip rates, while varying the rate at which filaments were reset to a refreshed, unstressed state. Increasing filament recycling rates produced two striking changes in the long time response of the network.. First, increasing recycling rates could prevent strain thinning, network tearing and acceleration of network strain rates observed in the absence of recycling. As an example, for the network shown in Figure 4a, strain thinning and

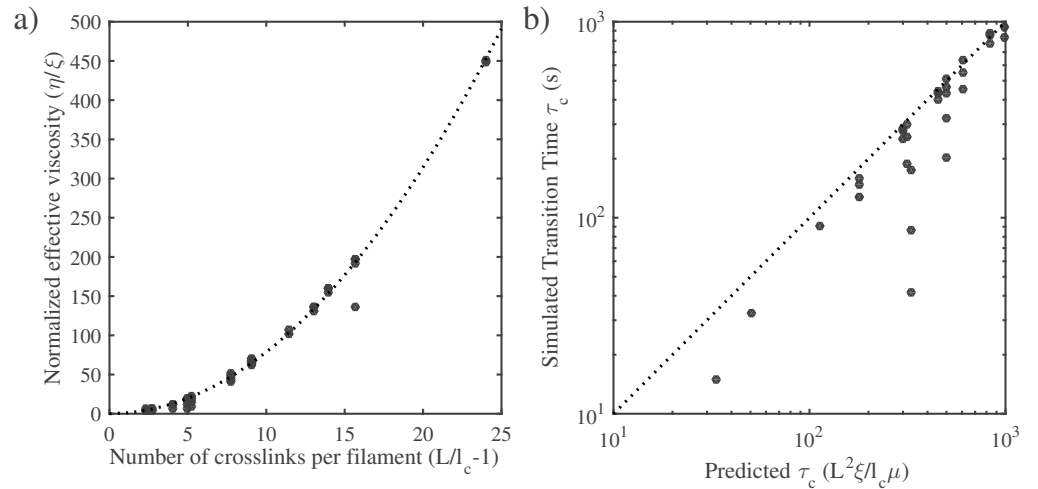


Figure 3. Network architecture sets the rate and timescales of deformation. **a)** The effective viscosity depends on the drag coefficient and the density of the network. Data points are the normalized effective viscosity from simulations (effective viscosity measured in fluid phase divided by the cross link friction coefficient) vs the number of cross links per filament ($L/l_c - 1$). Dotted line indicates the relationship predicted by a simple theory, $\eta_c = \xi(L/l_c - 1)^2$ **b)** The transition to viscous behavior occurs at a characteristic time, τ_c , that is set by the ratio of the elastic modulus predicted in [Head et al., 2003] (i.e. $G_0 \approx \mu/l_c$) to the effective viscosity, η_c .

network tearing lead to a rapid increase in strain rate above a critical strain of $\sim 40\%$. In contrast, when filaments are made to recycle with an average lifetime of 10 s, the same network, in response to the same level of applied stress, can sustain effectively viscous deformation, at a much higher strain rate (i.e. a much lower effective viscosity), for an indefinite period of time. Plotting effective viscosity as a function of decreasing recycling times revealed sharp decrease in effective viscosity as the recycling time approached τ_c , the characteristic time for transition to viscous deformation.

An intuitive explanation of this effect is that rapid recycling increases the network's ability to sustain the faster deformation rate that occurs during the initial viscoelastic response to applied stress. By constantly turning over strained network elements and replacing them with unstrained filaments, the network is able to dissipate stored elastic stress to maintain itself indefinitely within the viscoelastic response regime.

To test if this is a general relationship, we plotted the normalized effective viscosity (ratio of effective viscosity with recycling to effective viscosity without recycling, η_c) vs a normalized recycling rate (recycling time scaled by τ_c) for a large range of different network parameters and filament recycling times (Figure 8). Indeed, for a large range of network parameters, the normalized effective viscosity begins to decrease when the recycling time falls below τ_c and below this value the effective viscosity falls off linearly with recycling time.

Taken together, our results for the passive network under extension suggest that the passive stress relaxation of our network model is modified strongly by the presence of filament recycling. Given high enough levels of recycling, we find that network tearing can be prevented and that a steady state effective viscosity is established. Our model also suggests a simple microscopic derivation of viscosity which depends on the strength of inter filament cross-linking, the networks architecture, and the timescale of filament recycling.

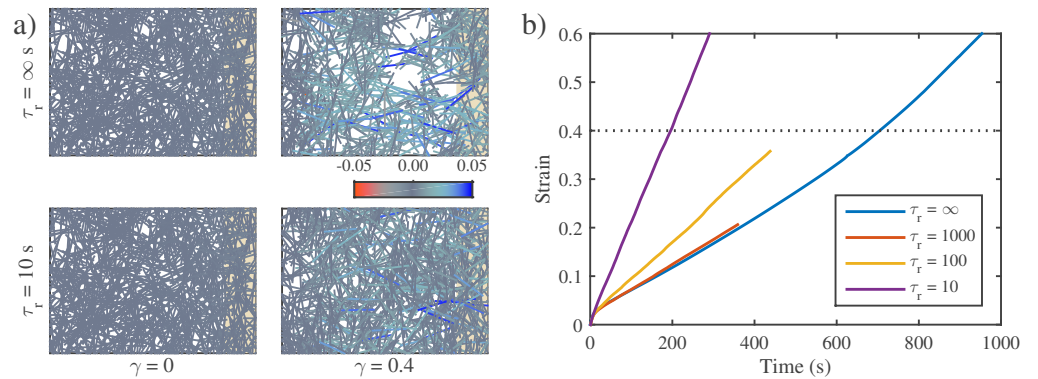


Figure 4. Filament recycling rescues network tearing and modulates effective viscosity. **a)** Examples of $20 \times 12 \mu\text{m}$ network under $0.001 \text{ nN}/\mu\text{m}$ extensional stress with recycling ($\tau_r = 10 \text{ s}$) and without, ($\tau_r = \infty$). Both images are taken when the patches had reached a net strain of 0.4. The network with recycling doesn't appear to change shape because its components have been recycled to remain in the original domain. Network parameters: $L = 3 \mu\text{m}$, $l_c = 0.5 \mu\text{m}$, $\xi = 10 \text{ nN} \cdot \text{s}$. **b)** Strain buildup for networks with parameters as in **a)** in the presence of different filament recycling rates. Dotted line indicates the strain state at which the snapshots in panel **a)** were taken. Note that the strain rate for $\tau_r = 1000$ is essentially identical to that of $\tau_r = \infty$, indicating that recycling does not govern the relaxation rate if the recycling time is above a threshold.

Filament recycling allows persistent stress buildup in active networks

In the absence of filament recycling, active networks with free boundaries contract and then stall against passive resistance to network compression. We found that our simulation axioms were able to produce transient contraction of a patch of free-floating network. As shown in Figure 5a, when an initially unstrained network has internal motor activity "switched on" at $t = 0$, the . By 100 s, the network has contracted by 40%, and many internal filaments can be seen to have reached a compressed state (indicated by orange). By 150 s, the compression has stalled, but filament sliding has begun to force some filaments away from the center. Over long time periods, this filament sorting actually rearranges the entire network, undoing the initial contraction (see supplemental video).

By monitoring both the network and individual filament strains, as in Figure 5b, we see that the networks macroscopic deformation can be explained entirely by a buildup of internal compression on individual filaments. Due to the strong stiffness asymmetry, there is far more compressive strain than there is extension in the network. It is this asymmetry that generates the net contraction in a disordered network despite myosin activity being equally capable of generating both. The network contraction stalled over the same timescale as individual filaments, further indicating the essential role of filament compression in generating contractility.

The final contraction extent was strongly dependent on the magnitudes of both the filament stiffness asymmetry (i.e. the ratio of the extensional and compressive stiffnesses μ_e/μ_c) and the motor activity scale (v). As shown in Figure 5c, small stiffness asymmetries lead to less overall contraction, while larger asymmetries appear to reach asymptotic once they reach a ratio of ~ 100 . Additionally, contraction would only occur when there was fractional motor activity, $0 < \phi < 1$, (see supplement). Finally, we found that the contraction consistently stalled over a time scale, $\tau_m =$ (see

supplement), indicating that the network architecture also plays a role in setting the timescale of contraction. These findings of the minimal requirements for contractility are all in direct accordance with the theoretical predictions of [Lenz et al., 2012] and [Lenz, 2014]. In fact, we find that removing any single factor from this simulation framework leads to a loss of contraction, suggesting that this system may represent a minimal model of contractility.

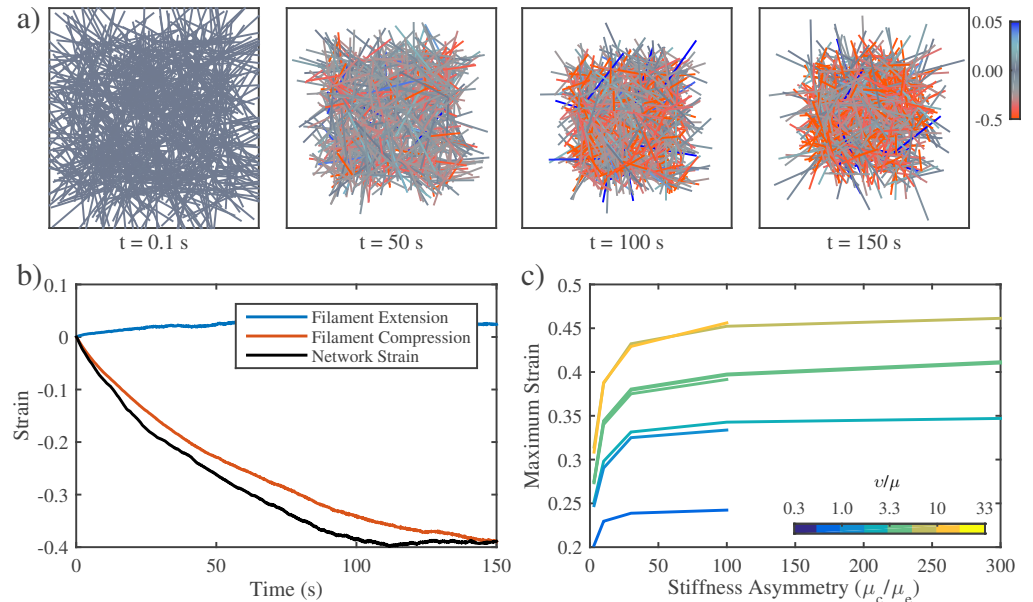


Figure 5. In the absence of filament recycling, active networks with free boundaries contract and then stall against passive resistance to network compression. **a)** Example of an active network contracting. Note the buildup of compressive stress as contraction approaches stall between 100 s and 150 s. Network parameters: $L = 5 \mu\text{m}$, $l_c = 0.3 \mu\text{m}$, $\xi = 100 \text{ nN} \cdot \text{s}$, $v = 0.1 \text{ nN}$. **b)** Plots showing time evolution of total network strain and the average extensional (blue) or compressive (red) strain on individual filaments. **c)** The network's ability to deform requires asymmetric filament compliance. Total network strain also increases with the applied myosin force v .

Active networks can only exert a transient force against a fixed boundary in the absence of filament recycling. Due to the complication of making measurements in the presence of such large-scale rearrangements of the network, we decided to additionally analyzed the stress buildup in a patch that was constrained to maintain its original area. The results from Figure 6a echo those from Figure 5a, with a consistent buildup of internal filament strain (represented by the colored lines) that stabilizes and persists indefinitely. However, in contrast the network in Figure 6a doesn't demonstrate any apparent large-scale rearrangement as any net deformation is impossible since the patch sets in a domain with periodic boundaries.

Under these conditions, we found that a net stress was generated throughout the material, but that the net stress could not be maintained and would decay after characteristic time. As shown in Figure 6b, the results showed a period of net stress due to an imbalance between larger stresses from extended filaments and smaller stresses from compressed filaments. After a characteristic timescale τ_a , the extensional stress peaks and begins to decrease while the compressive stresses continue to build up resulting in the extensional and compressive stresses beginning to cancel each other.

After this peak, the internal stresses become balanced and the net stress drops to approximately 0. Finally, we measured the time of peak stress and found it consistently occurred with a characteristic time, $\tau_a = \xi/l_c\sqrt{\mu v}$, as shown in Figure 6c.

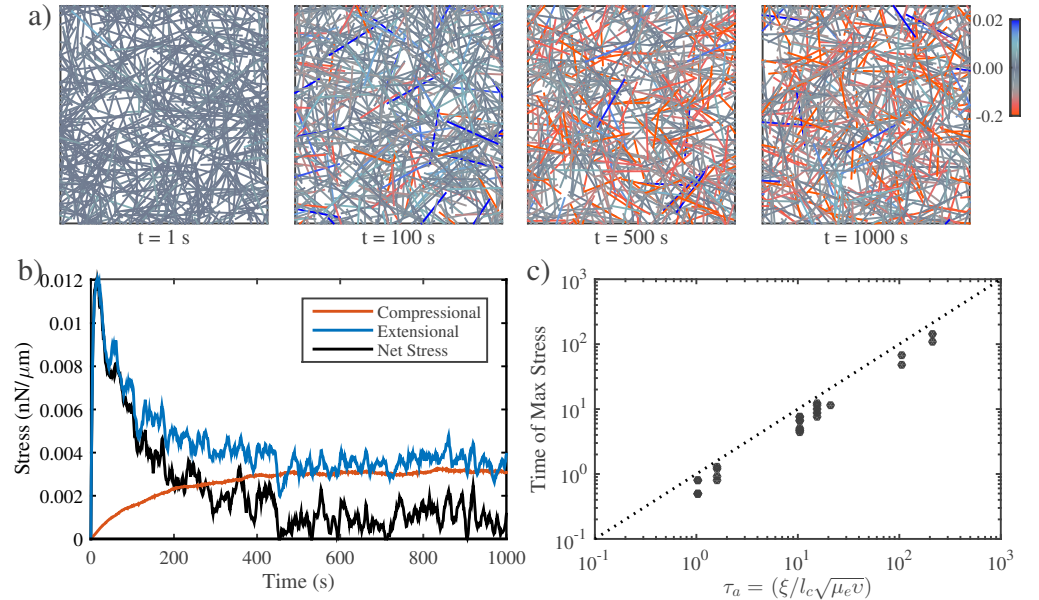


Figure 6. In the absence of filament recycling, active networks can only exert a transient force against a fixed boundary. **a)** Simulation of an active network with fixed boundaries illustrating progressive buildup of internal stress through local filament rearrangement and deformation. Note the progressive buildup of compressive stress on individual filaments. Network parameters: $L = 5 \mu m$, $l_c = 0.3 \mu m$, $\xi = 100 nN \cdot s$, $v = 0.1 nN$. **b)** Plots of total network stress and the average extensional (blue) and compressive (red) stress on individual filaments for the simulation shown in (a). Rapid buildup of extensional stress allows the network transiently to exert force on its boundary, but this force is dissipated at longer times as internal extensional and compressive stresses become balanced. **c.** Measurement and prediction of the characteristic time (τ_a) at which the maximum stress is achieved.

Filament recycling allows network to exert sustained stress on a fixed boundary. We next added filament recycling to the simulation setup and found that the presence of recycling allowed for persistent. Similar to the mechanism for preserving integrity in passive networks, the recycling appears to refresh the network such that subsets of filaments are continually transitioning from an unstressed to their stressed state before being recycled back to the unstressed state. The presence of recycling therefore both repaired structural inhomogeneities and reset the net strain of individual filaments. The panels in 7a show the differences in structure for identical starting architectures in the presence of different recycling timescales. Clearly, longer recycling times allow the network to reach a more strongly reorganized and internally stressed network.

Upon the addition of filament recycling, we found that the network maintained a nonzero net stress for timescales much longer than τ_a . We refer to this as the steady state stress because, based on our simulations, it doesn't appear that this stress ever subsides. As can be seen in Figure 7b, The profile of stress buildup changes dramatically by changing the recycling timescale in identical networks corresponding to

those in Figure 7a. It's important to notice that the effect of changing recycling time is not an entirely simple dependence. As the recycling time is decreased from 333 to 33.3, we can see that the long-term steady state increases from nearly 0.05 to a closer to 0.15. Nevertheless, the final steady state is still lower than the peak stress for those curves. In contrast, for the faster recycling rates (3.33, 0.33, 0.033), the final steady state decreases monotonically with decreasing recycling time. In addition, for these shorter timescales, the stress never reaches a peak but rather rises immediately to its steady state level. We attribute this to the strain resetting whereby individual filaments repeatedly are set to an unstrained state and then transition too having more strain until they are again reset.

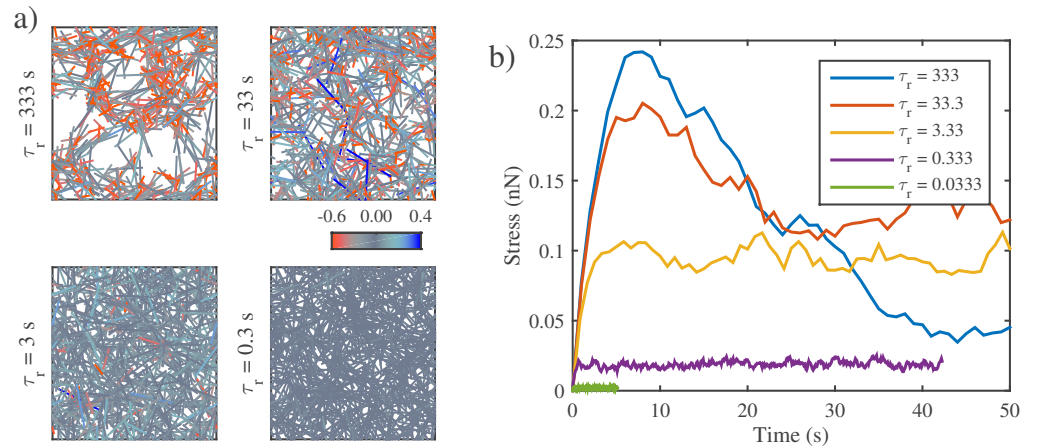


Figure 7. Filament recycling allows network to exert sustained stress on a fixed boundary. **a)** Example simulations of active networks and fixed boundaries for different timescales of filament recycling. Network parameters are the same as in Figure 6, except that the active force ($v = 1$) has been increased to emphasize the effects of internal network remodeling under stress. Note that significant remodeling occurs for longer recycling times. **b)** Plots of net stress for different recycling times; for long-lived filaments, stress is built rapidly, but then dissipates. Increasing filament turnover rates reduces stress dissipation by recycling compressed filaments; however, very short recycling times prevent any stress from being built up in the first place.

Filament recycling tunes the balance between active stress buildup and viscous stress relaxation to generate flows

We have shown that filament recycling has a strong impact on both passive and active properties of networks. However, we ultimately wish to show how filament recycling governs flows. Active fluid theories propose that flow can be explained in terms of the interplay between active stress and effective viscosity. Therefore, we next tested whether we could measure the effect of recycling on flow in networks with both an active and a passive domain.

Filament recycling tunes the magnitudes of both effective viscosity and steady state stress. To begin, we repeated the single domain (passive or active) simulations while varying all of our networks microscopic parameters. By exploring the effect of these parameters on the output variables we were able to determine the general form of the dependence. In Figure 8, we illustrate the data collapse of all our simulation results (See Supp. for details of parameter exploration). Interestingly, both

the viscosity and stress show different behaviors on either side of their respective governing timescales (τ_c for viscosity and τ_a for active stress). Effective viscosity was found to be independent of recycling time until recycling time became of the same order as the elastic to viscous crossover timescale, at which point it decreased with decreasing recycling time. Similarly, the steady state stress increases with increasing recycling time until it reaches the point of peak stress buildup. From that point it decreases with increasing recycling time.

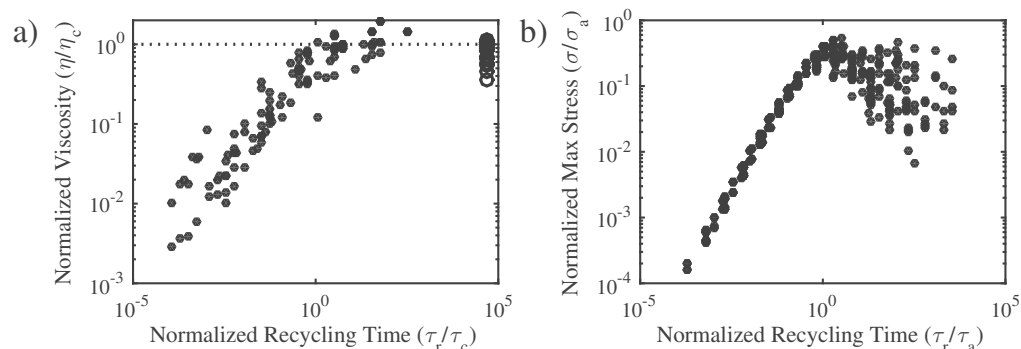


Figure 8. Filament recycling tunes the magnitude of effective viscosity and steady state stress. **a)** Normalized effective viscosities as a function of the normalized recycling time. When the recycling timescale is significantly less than the passive relaxation timescale (see Figure 3), the viscosity of the network becomes dependent on recycling time. **b)** Normalized steady state stress as a function of normalized recycling time. The steady state stress is set by the timescale at which the network strain is refreshed relative to the timescale at which the max stress is reached.

Filament recycling allows sustained flows in networks with non-isotropic activity.

Filament recycling enables flows and buffers changes in flow rate.

Supporting Information

Acknowledgments

We would like to thank Shiladitya Banerjee and Patrick McCall for stimulating discussions.

References

- Alvarado et al., 2013. Alvarado, J., Sheinman, M., Sharma, A., MacKintosh, F. C., and Koenderink, G. H. (2013). Molecular motors robustly drive active gels to a critically connected state. *Nat Phys*, 9(9):591–597.
- Banerjee and Marchetti, 2011. Banerjee, S. and Marchetti, M. C. (2011). Instabilities and oscillations in isotropic active gels. *Soft Matter*, 7:463–473.
- Banerjee et al., 2011. Banerjee, S., Marchetti, M. C., and Müller-Nedebock, K. (2011). Motor-driven dynamics of cytoskeletal filaments in motility assays. *Phys. Rev. E*, 84:011914.

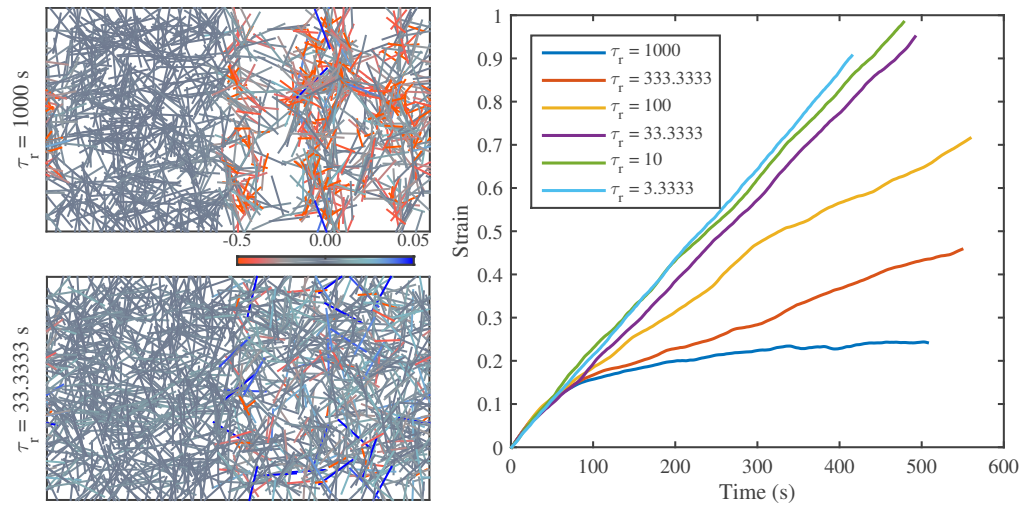


Figure 9. Filament recycling allows sustained flows in networks with non-isotropic activity. **a)** Example simulations of non-isotropic networks with long ($\tau_r = 1000$) and short ($\tau_r = 33$) recycling timescales. In these networks the left half of the network is passive while the right half is active. Network parameters: $L = 5 \mu m$, $l_c = 0.3 \mu m$, $\xi = 100 nN \cdot s$, $v = 1 nN$. **b)** Graph of strain for identical networks varying recycling timescales. With long recycling times, the network stalls; reducing the recycling timescale allows the network to persist in its deformation. However, for the shortest recycling timescales, the steady state strain appears to approach an asymptotic limit.

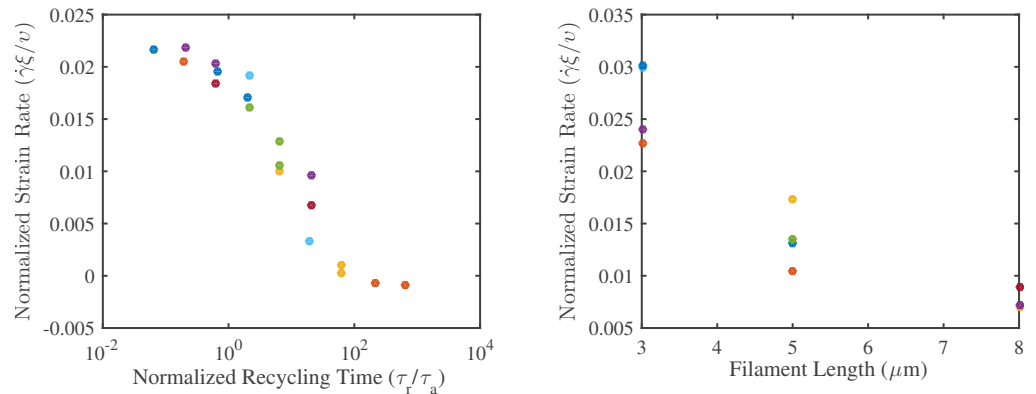


Figure 10

Bausch et al., 1998. Bausch, A. R., Ziemann, F., Boulbitch, A. A., Jacobson, K., and Sackmann, E. (1998). Local measurements of viscoelastic parameters of adherent cell surfaces by magnetic bead microrheometry. *Biophysical Journal*, 75(4):2038 – 2049.

Bois et al., 2011. Bois, J. S., Jülicher, F., and Grill, S. W. (2011). Pattern formation in active fluids. *Phys. Rev. Lett.*, 106:028103.

Bray and White, 1988. Bray, D. and White, J. (1988). Cortical flow in animal cells. *Science*, 239(4842):883–888.

Broedersz et al., 2010. Broedersz, C. P., Depken, M., Yao, N. Y., Pollak, M. R., Weitz, D. A., and MacKintosh, F. C. (2010). Cross-link-governed dynamics of biopolymer networks. *Phys. Rev. Lett.*, 105:238101.

-
- Broedersz et al., 2009. Broedersz, C. P., Storm, C., and MacKintosh, F. C. (2009). Effective-medium approach for stiff polymer networks with flexible cross-links. *Phys. Rev. E*, 79:061914.
- Chandran and Mofrad, 2010. Chandran, P. L. and Mofrad, M. R. K. (2010). Averaged implicit hydrodynamic model of semiflexible filaments. *Phys. Rev. E*, 81:031920.
- Dierkes et al., 2014. Dierkes, K., Sumi, A., Solon, J., and Salbreux, G. (2014). Spontaneous oscillations of elastic contractile materials with turnover. *Phys. Rev. Lett.*, 113:148102.
- Evans and Yeung, 1989. Evans, E. and Yeung, A. (1989). Apparent viscosity and cortical tension of blood granulocytes determined by micropipet aspiration. *Biophysical Journal*, 56(1):151–160.
- Filippov et al., 2004. Filippov, A. E., Klafter, J., and Urbakh, M. (2004). Friction through dynamical formation and rupture of molecular bonds. *Phys. Rev. Lett.*, 92:135503.
- Head et al., 2003. Head, D. A., Levine, A. J., and MacKintosh, F. C. (2003). Deformation of cross-linked semiflexible polymer networks. *Phys. Rev. Lett.*, 91:108102.
- Heisenberg and Bellaïche, 2013. Heisenberg, C.-P. and Bellaïche, Y. (2013). Forces in tissue morphogenesis and patterning. *Cell*, 153(5):948 – 962.
- Hiraiwa and Salbreux, 2015. Hiraiwa, T. and Salbreux, G. (2015). Role of turn-over in active stress generation in a filament network. *ArXiv e-prints*.
- Hird and White, 1993. Hird, S. N. and White, J. G. (1993). Cortical and cytoplasmic flow polarity in early embryonic cells of *caenorhabditis elegans*. *The Journal of Cell Biology*, 121(6):1343–1355.
- Hochmuth, 2000. Hochmuth, R. M. (2000). Micropipette aspiration of living cells. *Journal of Biomechanics*, 33(1):15 – 22.
- Keren et al., 2009. Keren, K., Yam, P. T., Kinkhabwala, A., Mogilner, A., and Theriot, J. A. (2009). Intracellular fluid flow in rapidly moving cells. *Nat Cell Biol*, 11(10):1219–1224.
- Kim et al., 2011. Kim, T., Hwang, W., and Kamm, R. D. (2011). Dynamic role of cross-linking proteins in actin rheology. *Biophysical Journal*, 101(7):1597–1603.
- Koenderink et al., 2009. Koenderink, G. H., Dogic, Z., Nakamura, F., Bendix, P. M., MacKintosh, F. C., Hartwig, J. H., Stossel, T. P., and Weitz, D. A. (2009). An active biopolymer network controlled by molecular motors. *Proceedings of the National Academy of Sciences of the United States of America*, 106(36):15192–15197.
- Köhler and Bausch, 2012. Köhler, S. and Bausch, A. R. (2012). Contraction mechanisms in composite active actin networks. *PLoS ONE*, 7(7):e39869.
- Lenz, 2014. Lenz, M. (2014). Geometrical origins of contractility in disordered actomyosin networks. *Phys. Rev. X*, 4:041002.
- Lenz et al., 2012. Lenz, M., Gardel, M. L., and Dinner, A. R. (2012). Requirements for contractility in disordered cytoskeletal bundles. *New Journal of Physics*, 14(3):033037.

-
- Lieleg and Bausch, 2007. Lieleg, O. and Bausch, A. R. (2007). Cross-linker unbinding and self-similarity in bundled cytoskeletal networks. *Phys. Rev. Lett.*, 99:158105.
- Lieleg et al., 2008. Lieleg, O., Claessens, M. M. A. E., Luan, Y., and Bausch, A. R. (2008). Transient binding and dissipation in cross-linked actin networks. *Phys. Rev. Lett.*, 101:108101.
- Lieleg et al., 2009. Lieleg, O., Schmoller, K. M., Claessens, M. M. A. E., and Bausch, A. R. (2009). Cytoskeletal polymer networks: Viscoelastic properties are determined by the microscopic interaction potential of cross-links. *Biophysical Journal*, 96(11):4725–4732.
- Liu et al., 2007. Liu, J., Koenderink, G. H., Kasza, K. E., MacKintosh, F. C., and Weitz, D. A. (2007). Visualizing the strain field in semiflexible polymer networks: Strain fluctuations and nonlinear rheology of *f*-actin gels. *Phys. Rev. Lett.*, 98:198304.
- Liverpool et al., 2009. Liverpool, T. B., Marchetti, M. C., Joanny, J.-F., and Prost, J. (2009). Mechanical response of active gels. *EPL (Europhysics Letters)*, 85(1):18007.
- Mak et al., 2016. Mak, M., Zaman, M. H., Kamm, R. D., and Kim, T. (2016). Interplay of active processes modulates tension and drives phase transition in self-renewing, motor-driven cytoskeletal networks. *Nat Commun*, 7.
- Marchetti et al., 2013. Marchetti, M. C., Joanny, J. F., Ramaswamy, S., Liverpool, T. B., Prost, J., Rao, M., and Simha, R. A. (2013). Hydrodynamics of soft active matter. *Rev. Mod. Phys.*, 85:1143–1189.
- Mayer et al., 2010. Mayer, M., Depken, M., Bois, J. S., Julicher, F., and Grill, S. W. (2010). Anisotropies in cortical tension reveal the physical basis of polarizing cortical flows. *Nature*, 467(7315):617–621.
- Müller et al., 2014. Müller, K. W., Bruinsma, R. F., Lieleg, O., Bausch, A. R., Wall, W. A., and Levine, A. J. (2014). Rheology of semiflexible bundle networks with transient linkers. *Phys. Rev. Lett.*, 112:238102.
- Munro et al., 2004. Munro, E., Nance, J., and Priess, J. R. (2004). Cortical flows powered by asymmetrical contraction transport {PAR} proteins to establish and maintain anterior-posterior polarity in the early *c. elegans* embryo. *Developmental Cell*, 7(3):413 – 424.
- Murrell and Gardel, 2012. Murrell, M. P. and Gardel, M. L. (2012). F-actin buckling coordinates contractility and severing in a biomimetic actomyosin cortex. *Proceedings of the National Academy of Sciences*, 109(51):20820–20825.
- Robin et al., 2014. Robin, F. B., McFadden, W. M., Yao, B., and Munro, E. M. (2014). Single-molecule analysis of cell surface dynamics in *caenorhabditis elegans* embryos. *Nat Meth*, 11(6):677–682.
- Salbreux et al., 2012. Salbreux, G., Charras, G., and Paluch, E. (2012). Actin cortex mechanics and cellular morphogenesis. *Trends in Cell Biology*, 22(10):536 – 545.
- Salbreux et al., 2009. Salbreux, G., Prost, J., and Joanny, J. F. (2009). Hydrodynamics of cellular cortical flows and the formation of contractile rings. *Phys. Rev. Lett.*, 103:058102.

-
- Sanchez et al., 2012. Sanchez, T., Chen, D. T. N., DeCamp, S. J., Heymann, M., and Dogic, Z. (2012). Spontaneous motion in hierarchically assembled active matter. *Nature*, 491(7424):431–434.
- Spruijt et al., 2010. Spruijt, E., Sprakel, J., Lemmers, M., Stuart, M. A. C., and van der Gucht, J. (2010). Relaxation dynamics at different time scales in electrostatic complexes: Time-salt superposition. *Phys. Rev. Lett.*, 105:208301.
- Turlier et al., 2014. Turlier, H., Audoly, B., Prost, J., and Joanny, J.-F. (2014). Furrow constriction in animal cell cytokinesis. *Biophysical Journal*, 106(1):114 – 123.
- Vanossi et al., 2013. Vanossi, A., Manini, N., Urbakh, M., Zapperi, S., and Tosatti, E. (2013). *Colloquium* : Modeling friction: From nanoscale to mesoscale. *Rev. Mod. Phys.*, 85:529–552.
- Wachsstock et al., 1994. Wachsstock, D., Schwarz, W., and Pollard, T. (1994). Cross-linker dynamics determine the mechanical properties of actin gels. *Biophysical Journal*, 66(3, Part 1):801 – 809.
- Ward et al., 2015. Ward, A., Hilitski, F., Schwenger, W., Welch, D., Lau, A. W. C., Vitelli, V., Mahadevan, L., and Dogic, Z. (2015). Solid friction between soft filaments. *Nat Mater*, advance online publication:–.
- Wilhelm and Frey, 2003. Wilhelm, J. and Frey, E. (2003). Elasticity of stiff polymer networks. *Phys. Rev. Lett.*, 91:108103.
- Yao et al., 2011. Yao, N. Y., Becker, D. J., Broedersz, C. P., Depken, M., MacKintosh, F. C., Pollak, M. R., and Weitz, D. A. (2011). Nonlinear viscoelasticity of actin transiently cross-linked with mutant alpha-actinin-4. *Journal of Molecular Biology*, 411(5):1062 – 1071.
- Zumdieck et al., 2007. Zumdieck, A., Kruse, K., Bringmann, H., Hyman, A. A., and Jülicher, F. (2007). Stress generation and filament turnover during actin ring constriction. *PLoS ONE*, 2(8):e696.